Deceleration, precooling, and multi-pass stopping of highly charged ions in Be^+ Coulomb crystals

L. Schmöger, M. Schwarz, T. M. Baumann, O. O. Versolato, B. Piest, T. Pfeifer, J. Ullrich, P. O. Schmidt, and J. R. Crespo López-Urrutia

Citation: Review of Scientific Instruments **86**, 103111 (2015); doi: 10.1063/1.4934245
View online: https://doi.org/10.1063/1.4934245
View Table of Contents: http://aip.scitation.org/toc/rsi/86/10
Published by the American Institute of Physics

Deceleration, precooling, and multi-pass stopping of highly charged ions in Be^+ Coulomb crystals

L. Schmöger,[1,2,a)] M. Schwarz,[1,2] T. M. Baumann,[1] O. O. Versolato,[1,2,b)] B. Piest,[1] T. Pfeifer,[1] J. Ullrich,[2] P. O. Schmidt,[2,3] and J. R. Crespo López-Urrutia[1]
[1]*Max-Planck-Institut für Kernphysik, Saupfercheckweg 1, 69117 Heidelberg, Germany*
[2]*Physikalisch-Technische Bundesanstalt, Bundesallee 100, 38116 Braunschweig, Germany*
[3]*Institut für Quantenoptik, Leibniz Universität Hannover, Welfengarten 1, 30167 Hannover, Germany*

(Received 15 July 2015; accepted 8 October 2015; published online 26 October 2015)

Preparing highly charged ions (HCIs) in a cold and strongly localized state is of particular interest for frequency metrology and tests of possible spatial and temporal variations of the fine structure constant. Our versatile preparation technique is based on the generic modular combination of a pulsed ion source with a cryogenic linear Paul trap. Both instruments are connected by a compact beamline with deceleration and precooling properties. We present its design and commissioning experiments regarding these two functionalities. A pulsed buncher tube allows for the deceleration and longitudinal phase-space compression of the ion pulses. External injection of slow HCIs, specifically Ar^{13+}, into the linear Paul trap and their subsequent retrapping in the absence of sympathetic cooling is demonstrated. The latter proved to be a necessary prerequisite for the multi-pass stopping of HCIs in continuously laser-cooled Be^+ Coulomb crystals. © *2015 AIP Publishing LLC.* [http://dx.doi.org/10.1063/1.4934245]

I. INTRODUCTION

Astrophysical observations of quasar absorption systems suggest a spatial dipole in values of the fine structure constant α across cosmological distances.[1] This result directly maps onto a present-day time variation of α due to the Earth's movement in the Universe on the order of 10^{-19}/yr and thus would in principle be verifiable in laboratory tests.[2]

Comparisons of frequency measurements between two or more atomic clock transitions that have different sensitivities to α variation can be used to set limits on temporal drifts of its value. Atomic frequency references based on trapped singly charged ions or neutral atoms have demonstrated systematic frequency uncertainties from 10^{-17} to 10^{-18} range.[3–6] Today's best constraint on alpha variation based on the clock-comparison method is an impressive[4] $\dot{\alpha}/\alpha = -2.0(2.0) \times 10^{-17}$/yr, not yet limiting the aforementioned astrophysical claims. Novel optical clocks based on transitions in highly charged ions (HCIs) would provide two advantages over singly charged atoms.

When increasing the charge state from a singly to highly charged ion the remaining electronic wavefunction is more compact, leading to strong relativistic effects accompanied by an enhanced sensitivity to α variation. Further, the strongly bound optically active electron leads to a low polarizability. HCIs are thus more immune to environmental changes due to their lower susceptibility to external field shifts. In addition, they offer narrow forbidden transitions in the optical wavelength regime which can appear, e.g., due to level crossings.[7] The associated high quality factor of the clock transition enables the development of novel optical frequency standards with projected natural fractional accuracies below the 10^{-19}–10^{-20} level[8,9] and sensitivity to α variation for transitions in HCIs approaches 10^{-20}/yr.[10,11] Some HCIs, such as Ir^{17+}, hold the possibility to realize two frequency references with large sensitivities to α variation of opposite sign within one ion, further enhancing the sensitivity.[7,12] Finally, HCIs offer many species suitable for the development of ultra-precise clocks and search for variation of fundamental constants.[9]

It would be desirable to apply high-precision laser spectroscopy to HCIs in order to exploit their advantageous properties. As a prerequisite, the HCIs have to be prepared in a cold and strongly localized state in a well-controlled environment. Achieving this objective is a challenge, since HCI production usually is an energetic process, either achieved by electron impact ionization or electron stripping,[13,14] which both leave the produced HCI ensemble at translational temperatures on the order of MK and direct laser cooling is usually not possible.

We use an electron beam ion trap (EBIT) as a HCI source, which is well suited for highly efficient electron impact ionization. Resonant fluorescence laser spectroscopy with HCIs *in situ* in an EBIT has been proven to be a valuable method for transition frequency determinations.[15,16] Measurement uncertainties for frequency determination of the ground state fine structure splitting down to 400 MHz were achieved in the case of the $^2P_{3/2}$–$^2P_{1/2}$ M1 transition in Ar^{13+} with the help of forced evaporative cooling of the HCI cloud.[15] However, evaporative cooling in EBITs is based on loosing HCIs from the trap and is thus fundamentally limited. The lowest temperatures accomplished with evaporative cooling were on the order of 12 eV for a Fe^{13+} ensemble, corresponding to a Doppler width of 20 GHz of the studied $^2P_{3/2}$–$^2P_{1/2}$ M1 transition,[16] whose natural linewidth is only 10 Hz. To

a)Electronic address: lisa.schmoeger@mpi-hd.mpg.de
b)Current address: ARCNL, Science Park 110, 1098 XG Amsterdam, The Netherlands.

overcome this drawback of in-EBIT HCI laser spectroscopy, we separate the hot production process from the cooling and spectroscopy trap. External ion injection methods have been frequently used for Paul trap β-decay and Penning trap mass measurements with accelerator-produced singly charged ions. There, the external ion injection techniques are based on cooling through collisions with a neutral buffer gas.[17–21] This technique is not available for HCI work due to losses by charge exchange. Other work regarding external HCI injection into Penning traps relies on resistive cooling[22–24] or proposed electron cooling.[25] These techniques are limited in achievable ion temperatures or not applicable in Paul traps, which are the working horse for the highest accuracy spectroscopy to date.

Thus, we employ sympathetic cooling[23,24,26,27] of HCIs through collisions with singly charged and continuously laser-cooled Be^+ ions that transfer energy from the injected slow HCI to the cold Be^+ ions. For this purpose, we have built a cryogenic linear Paul trap CryPTEx[28] and interfaced it with an ion source for HCI production through a deceleration and precooling beamline, as depicted in Fig. 1.

HCIs with charge state Q are produced in and extracted from the EBIT in pulsed mode with total mean kinetic energies on the order of 700 eV/Q and longitudinal FWHM energy spreads on the order of 25 eV/Q, due to the ion temperature within the production trap. This is equivalent to 2% of the HCIs having kinetic energies within a ±0.3 eV/Q interval around the mean kinetic energy, assuming a Gaussian distribution of their longitudinal kinetic energies. Subsequently we use a three-step deceleration and cooling process to confine and co-crystallize the HCIs in a microscopic region of our Paul trap. First, the HCI bunches, in particular Ar^{13+}, are decelerated and precooled by means of two serrated interlaced electrodes based on the pulsed drift tube (PDT) principle. Next is an electrostatic deceleration step performed by placing all Paul trap electrodes on a common retarding potential, which further decreases the kinetic energies below 1 eV/Q. This allows us to recapture the HCIs in the Paul trap. Finally, the motion of the HCIs is stopped by the frictional force which stems from Coulomb interactions with a laser-cooled Coulomb crystal of Be^+ ions. Eventually, the Ar^{13+} ions end up embedded in this crystal at residual kinetic energies below 2.4 μeV/Q (240 mK).[27] Hence, the Be^+ Coulomb crystal previously prepared in the Paul trap is used for both stopping of the HCIs motion and sympathetically cooling them into a crystallized state.

The presented preparation method is well-suited for other HCIs with similar mass-to-charge ratios and may allow us to study them in a well-controlled environment in the near future. Single crystallized HCIs may become amenable to quantum logic interrogation,[29] a technique used in some of the most accurate ion clocks.

This paper is structured as follows: Section II discusses the HCI extraction process from an EBIT, the need for a multi-pass stopping approach and gives estimates for the desired final kinetic energy of the extracted HCI pulses before they can be injected into the Paul trap. In Section III we motivate the need for phase-space manipulation of the extracted HCI bunches and describe the design and commissioning experiments regarding the pulsed deceleration and precooling properties of the beamline. Section IV details setup and scheme used for retrapping HCI bunches in the linear Paul trap, which is the necessary technical prerequisite that allows the multi-pass stopping of HCIs in Be^+ Coulomb crystals as described in Section V.

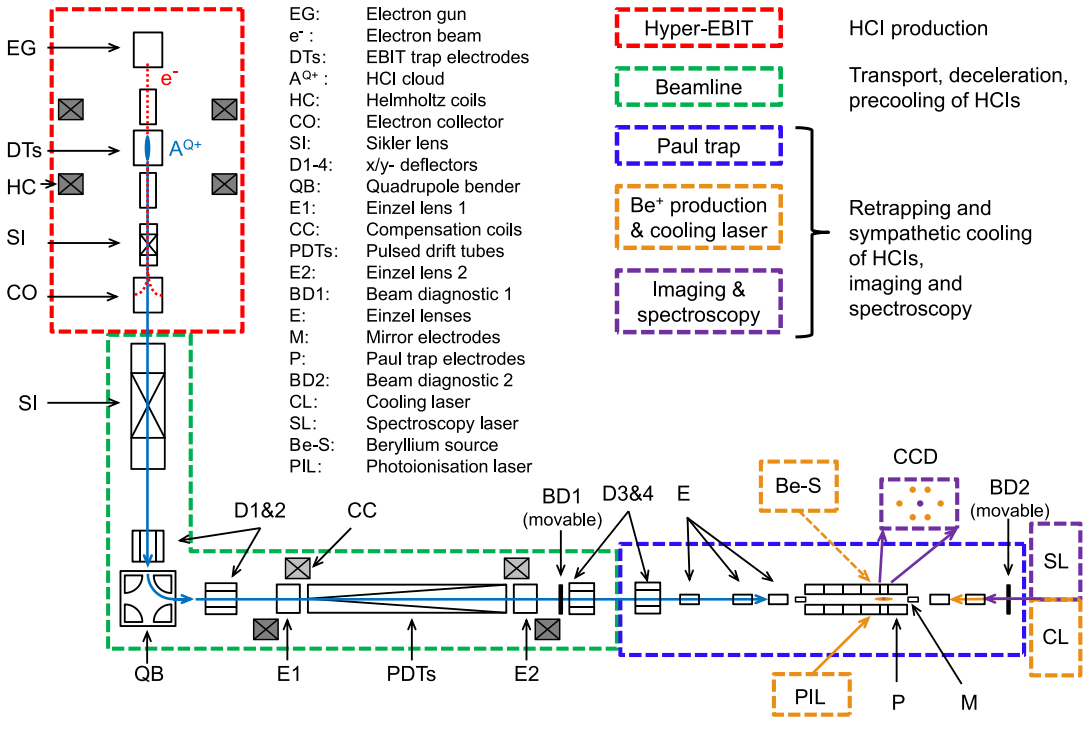

FIG. 1. Overview of the complete experimental setup used for the preparation of cold and strongly localized HCIs.

II. THEORETICAL BACKGROUND

A. Ion extraction from EBIT

The HCI ensemble is extracted from the EBIT in pulsed mode by switching the central trap electrode to a high positive potential V_{set}. The extraction potential V_{extr} does not equal the applied electrode potential. This is due to space charge effects V_{sc} of the electron beam and the fractional compensation χ of this effect due to the positively charged HCI cloud. The ion pulses start from an extraction potential V_{extr} given by

$$V_{extr} = (V_{set} + (1 - \chi)V_{sc})\kappa. \quad (1)$$

Ion extraction can start before the full value of V_{set} is reached. We introduce the parameter κ, which characterizes at which fraction of V_{set} the ions leave the trap, to account for this effect. A reasonably high extraction potential V_{extr} on the order of several kV for the pulsed extraction of HCI bunches from the EBIT is necessary in order to minimize the transverse emittance $\epsilon_{x/y,rms}$ of the ion pulses, which is a prerequisite for highly efficient HCI transport from the EBIT to the Paul trap. The transverse emittance for one subspace $\epsilon_{x/y,rms}$ due to the velocity distribution of the ions in the production trap is given by[30]

$$\epsilon_{x,rms} = \sigma_x \sqrt{\frac{k_B T_{HCI}}{2 Q_{HCI} V_{extr}}}. \quad (2)$$

T_{HCI} is the temperature of the HCI ensemble before extraction, k_B is Boltzmann's constant, and σ_x stands for the average transverse spread in position space of HCIs with charge state Q_{HCI}. The magnetic field contribution to the transverse emittance is small for extraction from EBITs, making Eq. (2) an estimate of the total transverse emittance for one subspace.[30] $\epsilon_{x/y,rms}$ can be minimized by evaporative cooling or minimization of heating due to electron-ion collisions (reducing the EBIT electron beam current). Additionally, σ_x could be reduced by increasing the EBIT magnetic field. The tuning range of σ_x and T_{HCI} is limited for a given setup. Thus, V_{extr} is the parameter of choice for minimizing the transverse emittance for high efficiency HCI transport. HCI pulses are extracted in the present case with typical mean kinetic energies of about $V_{extr}/Q_{HCI} = 680\ \text{eV}/Q_{HCI}$ and FWHM energy spreads of $25\ \text{eV}/Q_{HCI}$, in contrast to typical Ar^{13+} Paul trapping potential depth on the order of several eV to a few 10 eV. This calls for decreasing the kinetic energy of the extracted Ar^{13+} bunches by at least two orders of magnitude. In addition, the kinetic energy spread of the extracted HCI bunches needs to be reduced to match the energy emittance of the EBIT to the acceptance of the Paul trap. This enhances the stopping probability of HCIs during one retrapping cycle, which accelerates HCI loading and relaxes injection conditions of the HCI beam.

B. Stopping power of Be^+ Coulomb crystals

Decelerated HCI bunches injected into the linear Paul trap will lose their small residual kinetic energy by Coulomb collisions with prestored Be^+ ions, equivalent to a frictional force acting on the traversing HCIs. This retarding force can be expressed in terms of a stopping power of the Be^+ ion plasma as follows[31]:

$$-\frac{dE_{HCI}}{ds} = \frac{Q_{HCI}^2 e^2}{4\pi\epsilon_0} \frac{1}{v_{HCI}^2} \omega_p^2 \Lambda_C(E_{HCI}). \quad (3)$$

Equation (3) is derived from integrating the energy loss for a single collision with impact parameter b over all possible impact parameters. The energy loss $-dE_{HCI}/ds$ of the projectile HCI per distance s traveled in the target medium can be seen as consisting of three multiplicative terms. The first one includes the properties of the HCI projectile (e.g., Ar^{13+}), such as the charge state Q_{HCI} times the elementary charge e, the velocity v_{HCI} of the HCI and the vacuum permittivity ϵ_0. The second term is based on the plasma frequency ω_p of the target medium of charge state Q_T and mass M_T, which acts as a time scale for the response of the Be^+ ion plasma of a certain density n_T to the incoming HCI. The plasma frequency is given by

$$\omega_p = \sqrt{\frac{Q_T^2 e^2}{\epsilon_0 M_T} n_T}. \quad (4)$$

The third term is the so called Coulomb logarithm $\Lambda_C = \int_{b_{min}}^{b^{max}} \frac{db}{b}$, which is usually only weakly dependent on the HCI kinetic energy. We employ the formula

$$\Lambda_C = ln\left(\frac{\sqrt{128}\pi\epsilon_0 E_{HCI}^{3/2}}{Q_{HCI} Q_T e^2 M_{HCI}^{1/2} \omega_p}\right) \quad (5)$$

given by Bussmann *et al.*[31] to calculate Λ_C.

A coarse estimate for the upper limit on the initial kinetic energy of incoming HCIs can be obtained by calculating the plasma frequency for the laser-cooled Be^+ ion ensemble. The inverse of the plasma frequency sets the time scale for the response of the Be^+ ion target plasma to the HCI as incoming projectile. The Be^+ ion density $n_T = \epsilon_0 M_T \left(\omega_x^2 + \omega_y^2 + \omega_z^2\right)/Q_T$ can be deduced from the measured Paul trap frequencies $(\omega_x, \omega_y, \omega_z)$ in radial and axial directions, respectively. Typical trap frequencies of $(\omega_x, \omega_y, \omega_z) = 2\pi\,(188, 200, 115)$ kHz for our setup yield Be^+ target densities on the order of 2×10^{13} m^3 resulting in a plasma response time scale $\tau_p = \omega_p^{-1}$ of 400 ns. The interaction time t_i of the HCI with the Be^+ ion ensemble should be of the same order of magnitude as the plasma response time scale for efficient collective stopping of HCIs. Without decelerating Ar^{13+} bunches coming from the EBIT with typical kinetic energies of $680\ \text{eV}/Q_{HCI}$ are too fast to lose kinetic energy due to collective Coulomb interactions with the Be^+ ions, yielding an interaction time of $t_i = l/v_{HCI}$, where l is the length of the Be^+ Coulomb crystal and v_{HCI} the velocity of the HCI bunch. This results in an exemplary single-pass interaction time of Ar^{13+} with a 2 mm-sized Be^+ Coulomb crystal of about 10 ns. Following this coarse estimate the initial velocity of the HCIs should be decreased roughly by a factor of 40 before injection into the laser-cooled Be^+ ion ensemble. This corresponds to an initial HCI kinetic energy of about $0.5\ \text{eV}/Q_{HCI}$ (e.g., for Ar^{13+}: 6.5 eV).

Another estimate stems from Eq. (3). Here, in a very simple approach one neglects the weak kinetic energy dependence

of the Coulomb logarithm altogether and rewrites the stopping formula to read $-dE_{\mathrm{HCI}}/ds = f/E_{\mathrm{HCI}}$, where the factor f is the stopping power multiplied by the HCI projectile energy. Integrating this equation yields the relationship $E^2_{\mathrm{HCI\ initial}} = 2fs_{\mathrm{stop}}$ between the stopping length s_{stop} and the initial energy $E_{\mathrm{HCI\ initial}}$ of the HCI at injection. In this derivation, we assume that the Be^+ ensemble stay crystallized during the interaction with the HCIs and does not undergo a phase transition to the cloud- or fluid-like state. We calculate the stopping length for an initial energy of 1 eV for the example of stopping Ar^{13+} ions in a Be^+ Coulomb crystal to be about 130 mm ($\Lambda_C = 11.4$, $f = 3.8$ meV^2 μm^{-1}). This estimate suggests the use of a multi-pass process for stopping of HCIs in our Be^+ Coulomb crystals.

III. DECELERATION BEAMLINE

A. Beamline components

A cut-away view of the beamline is shown in Fig. 2. All electrodes (except for the bender electrodes made of titanium) are machined from stainless steel and electropolished afterwards for well defined field and enhanced vacuum conditions. The beamlines electrodes are housed in two 160 CF (conflat) vacuum chambers with overall dimensions of 0.7 m × 1 m. The vacuum is kept at 5×10^{-10} mbar by two 300 l s^{-1} turbo-molecular pumps backed by a 80 l s^{-1} turbo-molecular pump followed by a scroll fore-pump to render charge exchange losses negligible.

Following the path of the ions after extraction from the EBIT, they first encounter a 232 mm long Sikler lens[32] ((Sl) in Figs. 1 and 2). This is an adaptation of a three hollow cylinder Einzel lens, whose central electrode is cut twice diagonally to segment it into four electrodes. This allows for focusing and two-dimensional steering of the ion bunches with least aberrations. Next are four steerer electrodes ((D1) in Figs. 1 and 2) which originate from a hollow cylinder which is cut twice orthogonally along its symmetry axis. One of these four electrodes is used as a kicker electrode for active charge state selection. The 90° deflection of the ions in the direction of the Paul trap is performed by an electrostatic quadrupole bender ((QB) in Figs. 1 and 2), which consists of two negatively and two positively biased electrodes in a grounded housing.[33] The rectangular entrance and exit apertures of the bender have dimensions of 12 mm × 52 mm. This bender design has been preferred over a cylindrical concept, because it allows for switching between two separate ion sources and provides optical access for cooling and spectroscopy lasers without introducing field distortions as in cylindrical benders. The astigmatism induced by the deflector into the ion bunches can be corrected for through the use of electrodes (D2) (see Figs. 1 and 2), whose electrode geometry is identical to (D1). The difference to (D1) in functionality stems from the voltages applied to the electrodes. For astigmatism correction two opposing electrodes are placed at the same potential V, while the orthogonal electrode pair is placed at $-V$. Both 39 mm long three-cylinder Einzel lenses ((E1) and (E2) in Figs. 1 and 2) focus the ion pulses before and after their deceleration. Calculations of space charge effects in the extracted ion pulses showed the need for focusing along the beam path even in the absence of initial beam divergence. An ion pulse with an initial diameter of 4 mm and 5×10^4 Ar^{13+} ions in the pulse would have a beam diameter of about 45 mm at the end of the beamline. This value is greater than the 40 mm inner diameter of the beamline electrodes.

The main element of the beamline is the deceleration unit ((PDTs) in Figs. 1 and 2). It is formed by two interlaced serrated electrodes that work according to the pulsed drift tube principle[34,35] and allows for deceleration and precooling of the extracted ion bunches. Its operation will be detailed below.

A movable ion detector in combination with a retarding field analyzer ((BD1) in Fig. 1) is placed at the end of the

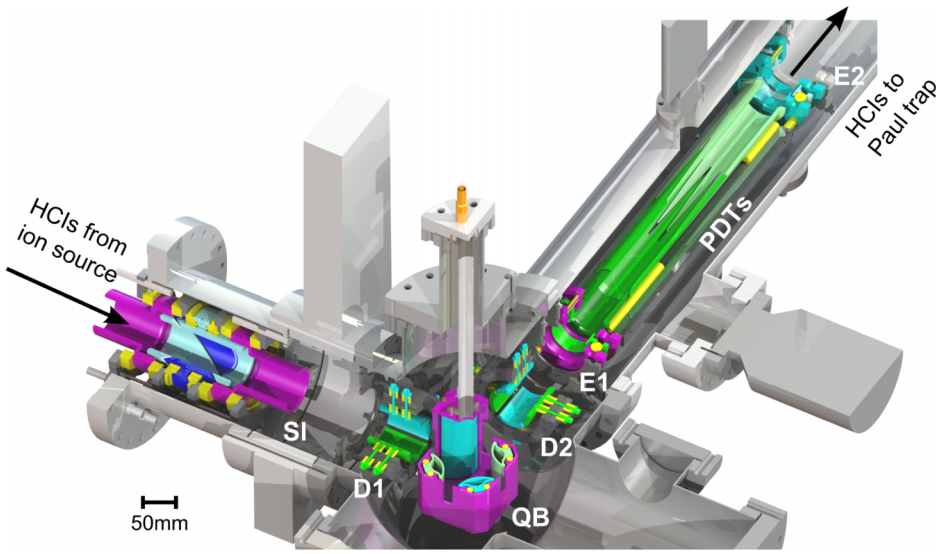

FIG. 2. Cross-section of deceleration beamline. Components: (Sl) Sikler lens, (D1) deflector electrodes — the blue one is used as a kicker electrode, (QB) electrostatic quadrupole bender, (D2) deflector electrodes,(E1) and (E2) Einzel lenses, (PDTs) two serrated pulsed drift tubes for deceleration and precooling of HCI bunches. Magenta electrodes are held at ground potential, blue electrodes are negatively biased, green electrodes are positively biased. EBIT residual magnetic field compensation coils are not shown here.

beamline (directly behind (E2)). It consists of two microchannel plates (MCPs) in Chevron configuration[36] together with two copper grids directly in front of the actual MCP ion detector. The first grid is on ground potential, while the retarding potential V_G of the second one can be linearly increased until the number of detected ions N_{ions} decreases to zero. We perform a Boltzmann fit of these data and take its 1st derivative to determine the kinetic energy distribution of the ions in the extracted bunches. This is possible since the number of ions with charge Q detected behind the retarding grid equals the convolution of the true kinetic energy distribution $B(E_{kin})$ of the ion bunch with the Heaviside function $\Theta(E_{kin} - QV_G)$ for an ideal retarding field analyzer. Assuming a Gaussian longitudinal kinetic energy distribution we measure a FWHM on the order of 25 eV/Q for Ar^{4+}-Ar^{14+} at typical mean kinetic energies of $\bar{V}_{extr}$ = 680 eV/Q without deceleration.

A second movable ion detector ((BD2) in Fig. 1) based on two MCPs in Chevron configuration is located behind the Paul trap. Its front plate is biased to −2.2 kV, its back plate to −200 V and the metal anode used for readout is held at ground potential.

B. Pulsed buncher tube — Working principle

Extracting HCIs from the EBIT in pulsed mode allows for deceleration by an electrodynamical instead of an electrostatic deceleration setup with the advantage that one is not constrained by Liouville's theorem[37] and no high voltage platform for the Paul trap is needed. We can place the two serrated electrodes (PDT1 and PDT2) of the deceleration unit on the same positive potential, resulting in a decelerating potential hill. The ions lose kinetic energy when climbing up the retarding potential until they are inside the long electrode structure. While the ion bunch travels through the electrodes their voltages are simultaneously switched over a range that equals the initial ion energy (divided by Q), so that the ion pulse exits the system with lower mean kinetic energy. The kinetic energy spread of the HCI bunch is conserved through this deceleration process. Without pulsing down the electrode voltages the ions would have gained kinetic energy again when rolling down the potential hill at the end of the electrodes.

In addition to decelerating ion bunches, the deceleration unit ((PDTs) in Fig. 2) can be used to simultaneously reduce their longitudinal kinetic energy spread, as illustrated schematically in Fig. 3. This is done by placing both serrated interlaced electrodes on different potentials. The first one (PDT1), as seen by the ions coming from the EBIT, is set on a lower voltage as the second one (PDT2): $V_{PDT1} < V_{PDT2}$. This results in a linearly increasing retarding potential in the interlaced region of the teeth of the two electrodes. Subsequently, at the arrival of a trigger TTL signal, both drift tubes are pulsed down quickly to ground while the ions of the bunch with former mean kinetic energy are in the middle of the interlaced region. Thus, the faster ions with higher kinetic energy have experienced a stronger decelerating potential at the pulse-down time than ions with former mean kinetic extraction energy $\bar{V}_{extr}$. The reversed considerations hold true for the slower ions in the bunch with lower kinetic energy, which are decelerated less than those with the mean kinetic

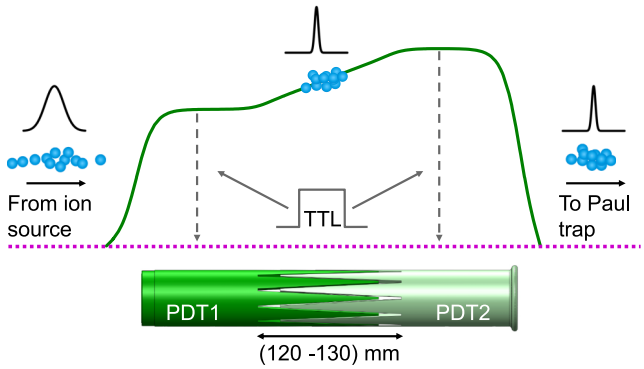

FIG. 3. Longitudinal phase-space compression of ion bunches by means of a pulsed linearly increasing deceleration potential (green curve). The voltages applied to both serrated electrodes are simultaneously pulsed to ground (dotted horizontal line), triggered by a common TTL signal. Black curves above ion bunches (blue spheres) are the corresponding schematic longitudinal kinetic energy distributions.

energy at the pulse-down time. The HCIs exit the system with a lower mean kinetic energy V_f as well as a reduced energy spread. The longitudinal phase-space compression by application of transient voltage pulses enhances the efficiency of the HCI stopping process in the laser-cooled Be^+ ensemble, due to the increased number of HCIs in the energy interval suitable for being stopped by the Coulomb interaction with Be^+ (see Section II).

This effect can only be achieved by using the correct pulse-down time and by applying specific combinations of voltages to the two serrated electrodes. Calculations, based on a one dimensional model of the ion motion along the axis, are used to get an estimate for suitable voltage combinations and to quantify the precooling process further.

C. Pulsed buncher tube — Theoretical model

Starting point for the calculation is a discretized assumed Gaussian distribution in longitudinal kinetic energy of the extracted HCI bunch. An exemplary ion energy distribution is shown in Fig. 4(b) with mean kinetic energy $Q\bar{V}_{extr}$ = 680 eV/Q and standard deviation QV_σ = 10.6 eV/Q, as typically measured for HCI bunches extracted from Hyper-EBIT. Here, we used Mathematica[38] to generate, e.g., 5000 pseudorandom variates from the assumed continuous Gaussian energy distribution. The motion of the i-th HCI in the bunch with longitudinal kinetic extraction energy of QV_i is modeled by three consecutive regions. The ion performs a uniform linear motion with velocity $v_i = \sqrt{2QV_i}/M$ in the first 1527 mm long region until the ion starts to enter the deceleration unit. This is followed by a second linear motion region with a length of 95 mm with decreased velocity $v_i = \sqrt{2Q/M(V_i - V_{PDT1})}$ and a motion with uniform deceleration $a = -Q(V_{PDT2} - V_{PDT1})/(Md)$ within the interlaced region of the two serrated electrodes with geometric length d. The retarding potential V_{ir} experienced by the i-th HCI at the common pulse-down time t_S is given by $V_{ir} = z_i(V_{PDT2} - V_{PDT1})/d + V_{PDT1}$, where z_i is the position of the specific ion within the interlaced region of PDT1 and PDT2 at t_S. So that the i-th HCI leaves the deceleration unit with longitudinal kinetic energy $V_i - V_{ir}$.

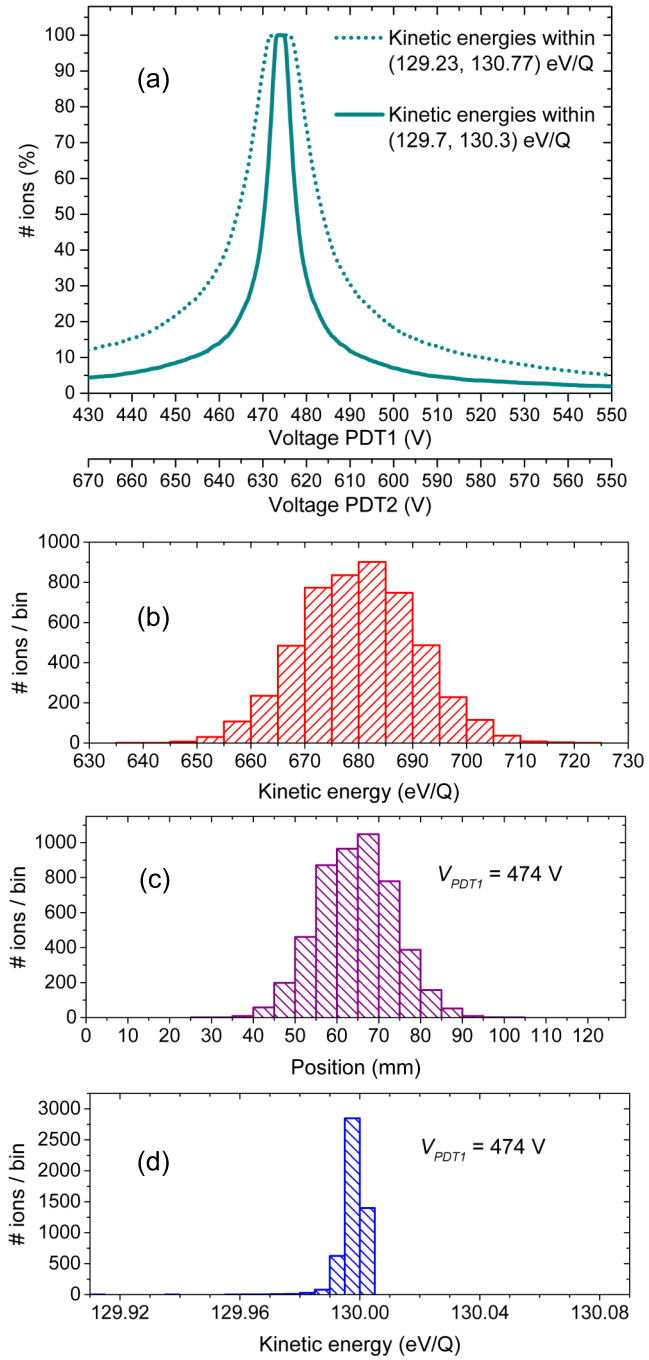

FIG. 4. Shown in (a) are calculations of the percentage of ions within specific kinetic energy intervals after deceleration over different voltage combinations of the two serrated electrodes (PDT1 and PDT2). The voltage applied to PDT1 determines the one applied to PDT2 through $(V_{PDT1}+V_{PDT2})/2 = \bar{V}_{\mathrm{extr}} - V_{\mathrm{f}}$ (This example: $\bar{V}_{extr} = 680$ V, $V_{\mathrm{f}} = 130$ V). The initial kinetic energy distribution in the extracted ion bunch used for these Mathematica calculations is depicted in (b). (c) Calculated longitudinal position distribution of the ion bunch within the 129 mm long interlaced region at pulse-down time. Assumed voltage of 474 V applied to PDT1. (d) Kinetic energy distribution after decelerating the ions with a voltage of 474 V applied to PDT1 (minimum achievable energy spread).

The calculated position distribution within the 129 mm long interlaced region is shown in Fig. 4(c) for a voltage of 474 V applied to PDT1 and a mean kinetic energy after deceleration of $QV_{\mathrm{f}} = 130\ \mathrm{eV}/Q$. QV_{f} has been chosen so that its value is experimentally suitable for the next deceleration process in the Paul trap. The resulting kinetic energy distribution after the deceleration process is depicted in Fig. 4(d). The voltage applied to PDT1 conditions the one applied to PDT2 through $(V_{PDT1} + V_{PDT2})/2 = \bar{V}_{\mathrm{extr}} - V_{\mathrm{f}}$. The histograms shown in Figs. 4(c) and 4(d) have been calculated for $V_{PDT1} = 474$ V, since this voltage yields the minimum energy spread after deceleration for the assumed starting conditions and given value of mean kinetic energy after deceleration. This minimal energy spread corresponds to a maximum value for the percentage p of ions in a particular kinetic energy interval after deceleration (Fig. 4(a)), which is the figure of merit for the deceleration unit. 90% of the decelerated ions are in a kinetic energy interval of $\pm 0.3\ \mathrm{eV}/Q$ around $130\ \mathrm{eV}/Q$ for voltages of 472.4 V–475.7 V applied to PDT1.

In conclusion, theoretically 100% of all Ar^{13+} ions in an extracted and decelerated HCI bunch have energies within a range of ±4 eV around $13 \times V_{\mathrm{f}} = 13 \times 130$ eV, if precooled by means of the linearly increasing decelerating potential defined by $V_{PDT1} = [473.5, 474.5]$ V. Decelerating to the same mean kinetic energy but without precooling (both serrated electrodes held at 550 V) results in only 2% of all Ar^{13+} ions within a range of ±4 eV around $13 \times V_{\mathrm{f}} = 13 \times 130$ eV. Thus, precooling yields an expected improvement by a factor of 50 for application of optimal pulsed drift tube voltages. This enhancement factor increases the probability for stopping of further electrostatically decelerated Ar^{13+} ions in a Be^{+} Coulomb crystal within one extraction cycle.

For steeper linearly increasing deceleration potentials, ions faster than the ions with former mean kinetic energy are decelerated to kinetic energies below those of the slower ions in the bunch. This starts to appear for $V_{PDT1} < 474$ V. Too steep decelerating potentials, produced by voltages applied to PDT1 that are smaller than 370 V for the given example, result in an increased energy spread in the decelerated HCI bunch compared to the initial energy distribution after extraction due to this reversing effect.

Main limitations of the theoretical model used for the deceleration process above stem from assuming that the electrode voltages are pulsed down to ground instantaneously, from neglecting the transverse emittance of the HCI beam and from assuming a stepwise increase from ground to the retarding potential V_{PDT1}. SIMION[39] simulations including these effects do not show different results from the one-dimensional model qualitatively, but yield a different value for the maximal achievable value of p for the decelerated HCI pulse, as detailed in the next paragraphs.

The geometry of the deceleration unit, the neighbouring ion optics, and the surrounding vacuum chamber is modeled through a CAD model import into the SIMION simulation software. The distance between the starting position of the HCI bunches and (E1) (see Fig. 1) is based on our experimental geometry. A user program based on a scripting language is implemented to apply time-dependent voltages to the pulsed drift tube electrodes as the ions fly through them. As long as the mean time-of-flight (TOF) of a HCI bunch remains smaller than the pulse-down time t_{S} constant retarding potentials V_{PDT1} and V_{PDT2} are applied. SIMION starts to exponentially decrease the pulsed drift tube potentials with a time constant of $\tau = 0.11\ \mu$s when the mean ion TOF equals t_{S}. For this purpose, the ion time steps are synchronized exactly with the

pulse-down time. 5000 Ar^{13+} ions are flown with an initial kinetic energy distribution with the same mean and standard deviation as the one shown in Fig. 4(b) and their individual kinetic energies are recorded after the deceleration process at the end of the beamline ((BD1) in Fig. 1)). As a result, 96% of the decelerated ions have kinetic energies within ±4 eV around $13 \times V_f = 13 \times 130$ eV for $V_{PDT1} = 470$ V and $V_{PDT2} = 630$ V.

The value for the time constant τ comes from simulations using the software SPICE[40] of the potentials of the pulsed drift tubes through the pulse-down process. For these simulations we modeled the pulsed drift tubes as capacitances against each other (70 pF) and against the vacuum chamber (10 pF) and included the pulse-down electronics together with all used cables into the simulations. The pulse-down electronics are based on two fast high voltage transistor switches (Behlke HTS31) that are triggered synchronously by a delay generator when the HCI bunch is extracted from the EBIT. The time constants were verified experimentally by an oscilloscope which was included in the simulations.

Changing the starting conditions of the HCI in the SIMION simulation, so that the ions are distributed over 6.5 mm diameter around the symmetry axis of the PDTs does not affect the percentage of decelerated ions in the ±4 eV kinetic energy interval around 13×130 eV. This is in accord with the FEM simulation shown in Fig. 5(c). Here, the potential in a cut plane through the middle of the interlaced region is displayed, showing the spatially averaged potential probed by the ions for $V_{PDT1} = 450$ V and $V_{PDT2} = 650$ V. The deviation from the set averaged potential of 550 V is smaller than 0.1% within a geometric inner diameter of 22 mm. This effective inner diameter increases for an increasing number of teeth when the geometric inner diameter is kept constant. But a high teeth number becomes difficult to machine, so that 10 of them have been chosen for the current setup. The deviation between simulated and expected radii that affect p stems from the electrostatic lensing effect of the pulsed drift tubes.

Adding a cone direction distribution with a half-angle of 0.1° to the above starting conditions of the HCI in the SIMION simulation yields a value of $p = 88\%$, which can be increased to 94% by using the einzel lens (E1) to counteract the divergence in the ion beam.

No HCI losses on the way to detector (BD1) in Fig. 1 are observed for the above SIMION simulations of the longitudinal phase-space compressions of the Ar^{13+} ion bunches.

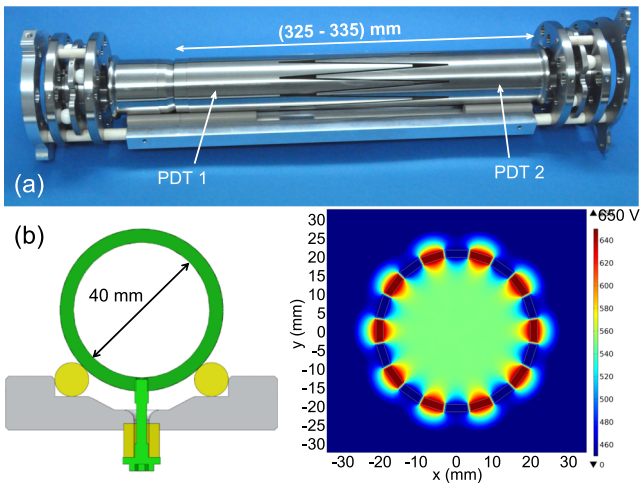

FIG. 5. (a) Photograph of the two mounted serrated deceleration electrodes (PDT1 and PDT2), together with the two Einzel lenses. (b) Mounting principle of the serrated electrodes. (c) FEM simulation of the electric potential in a cut plane through the middle of the interlaced region, showing the spatially averaged potential probed by the ions.

D. Pulsed buncher tube — design

The two serrated electrodes are produced through wire electrical discharge machining and rest on PEEK (polyether ether ketone) rods that insulate them against a common grounded aluminum mounting plate (Figs. 5(a) and 5(b)). The two electrodes are coaxially mounted within a tolerance of 50 μm. The insulating rods are 90° apart around the circumference of the serrated electrodes for maximum strength. The mounting scheme prevents charge up of the insulators by placing them outside the line of sight of the HCI bunches. Besides the number of teeth, specifications for building the deceleration unit consist of values for the overall length of the unit, the inner diameter of the electrodes, and the length of the linearly increasing potential. The latter is given by possible position distributions of the ions in the bunch inside the interlaced region. A value of 40 mm for the inner diameter has been chosen as a compromise between limiting aberrations in the ion beam, increasing the effective inner diameter and minimizing the overall length of the deceleration unit. The overall length is correlated with the inner diameter, since it determines the amount of electric field penetration from neighbouring electrodes into the pulsed drift tubes and thus the effective length of the unit.

In principle, a linearly increasing potential could also be produced with two hollow-cylinder electrodes on different potentials separated by a specific distance. However, limitations due to electric field penetration from the grounded vacuum chamber in the gap between the electrodes arise for distances comparable to the expected length of the ion pulses. Such a design would only be feasible for small separations and would thus not be suitable for precooling HCI bunches coming from the EBIT. Alternatively, several aperture electrodes in a row, separated with small distances (~1 mm), could be used to create an arbitrary increase in the decelerating potential. This however would result in complex electronics for simultaneously pulsing down all electrodes.

E. Commissioning experiments

1. *Ion identification and active charge state selection*

Continuously injecting neutral Ar atoms into the EBIT trapping region leads to the sequential production of argon charge states by electron impact ionization (EII). Besides EII, charge exchange and recombination processes are charge changing mechanisms in the EBIT ion plasma, as known from the rate equations that govern the ion population dynamics in an EBIT. Hence, extracted HCI pulses from an EBIT always contain several charge states of the injected neutral species meaning that only a fraction of the total ion yield is in a specified charge state.

Identification of all ions in the extracted pulses is a prerequisite for both the optimization of the ion source operating parameters (e.g., electron beam energy, charge breeding time, trap depth, injection pressure) to increase the yield of the ions of interest and their active selection from the bunch. The identification of the extracted ions is the first step in the commissioning of the beamline.

There are only electrostatic ion optic elements between the EBIT and the ion detector directly located behind the beamline. Thus, the ion identification could only be done by means of a time-of-flight method, where the whole beamline is a part of the 2 m distance z between the central trap electrode of the EBIT (center of (DTs) in Fig. 1) and the ion detector (BD1) (see Fig. 1). The time-of-fight spectrum of the extracted ion cloud is recorded by an oscilloscope, triggered by the same signal that triggers the pulsed extraction from the ion source. The zero of the oscilloscopes time scale marks the time where the ions simultaneously leave the EBIT, before they are charge-to-mass-ratio Q/M separated through their different time-of-flights. A typical TOF spectrum averaged over 64 extracted HCI bunches is shown in Fig. 6. In principle, the Q/M ratio of the separate peaks could be identified by means of the formula

$$\frac{Q}{M}\left[\frac{e}{\mathrm{u}}\right] \approx 1.04 \times 10^4 \frac{(z[\mathrm{m}])^2}{2V_{\mathrm{extr}}[\mathrm{V}](t[\mu\mathrm{s}])^2}, \qquad (6)$$

where t is the mean TOF of the HCI pulse with a specific Q/M and z is the distance traveled from the central EBIT trap electrode to the ion detector. Eq. (6) is derived from energy conservation for charged particles in electric fields under the assumption of uniform linear motion through the ion optics. All quantities in Eq. (6) are experimentally measurable.

However, Eq. (6) is based on the assumption of the HCI's uniform linear motion along z, which does not hold because of several electrostatic ion optic elements (Sikler lens, Einzel lenses) along the way. Due to energy conservation, electrostatic ion optics do not lead to a net change in ion velocity, but they result in a change of the measured TOF since the ions travel faster (slower) inside the negatively (positively) biased ion optical element. Further, this change in time-of-flight t is Q/M dependent as $t \propto (Q/M)^{-1/2}$. SIMION simulations of the ion optic TOF effects together with Eq. (6) allow a rough Q/M identification of the individual peaks in Fig. 6.

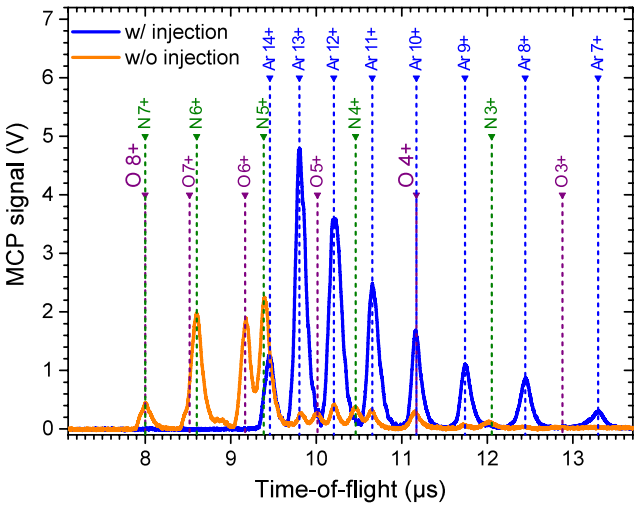

FIG. 6. Identification of ions with different Q/M contained in exemplary bunches extracted from the EBIT. Blue curve: averaged time-of-flight spectrum of extracted ion pulses with injection of neutral Ar into the trap prior to extraction. Orange curve: averaged time-of-flight spectrum of extracted ion pulses without injection of neutral Ar into the trap (valve to gas injector closed). Ion production EBIT settings: e^--beam current of 14 mA, e^--beam acceleration voltage of 900 V, inverted trap.

Those are unambiguously confirmed by the combination with other identification methods. One of them comprises of the comparison of a TOF spectrum taken with injection of the desired element with a TOF spectrum taken with turned off injection, as shown in Fig. 6. In the latter case the spectrum is dominated by different charge states of residual gas elements that are always present in an EBIT. When the injection of neutral Ar gas is turned on, those lighter ions are displaced from the trap and different charge states of argon are mainly produced. Another method consists of varying the energy of the nearly mono-energetic electron beam, observing the appearance of new peaks in the TOF spectrum and comparing the needed electron beam energy with the known ionization potentials of the element. In addition, we were able to use the observation of charge state distinct dielectronic recombinations[41,42] in argon to check the correctness of our Q/M identification.

After HCI identification, the desired Q/M peak is actively selected by suppressing surrounding charge states. Higher charge states are suppressed by choosing an electron beam energy below or near their ionization potential where production rates are low. Lower charge states are eliminated by using the kicker electrode (D1) in Fig. 2. A long high voltage pulse is quickly applied to this electrode after the HCI pulse with the desired charge state (e.g., 13 elementary charges) has passed the electrode. By doing so, pulses of lower Ar charge states are forced on a trajectory that does not allow them to enter the 12 mm wide entrance aperture of the quadrupole bender. An exemplary result of this active charge state selection is depicted in Fig. 7.

2. Decelerating and precooling HCI bunches

Figure 8 shows the scheme of the measurement principle used for commissioning the beamline. It is employed to test its deceleration properties and to experimentally determine suitable pulse-down times for the pulsed drift tubes. Two trigger signals with variable delay are generated by means of a delay generator, e.g., with a frequency of 2 Hz. One (magenta solid lines in Fig. 8) is used to extract the HCI cloud through quickly applying a high voltage pulse to the central trap electrode with the help of a Behlke switch. At the same time, this trigger signal is also used to set the zero point of the oscilloscopes time scale used to record the TOF spectrum. The other trigger signal (blue dashed lines in Fig. 8) is delayed by the pulse-down time t_S and is used to simultaneously pulsedown both serrated electrodes with the help of two Behlke switches. Varying t_S with a small step size (typ. 50 ns) and recording the TOF spectrum for each step allows for observing changes in the TOF of the different HCI charge states due to the deceleration process. t_S corresponds to a specific distance that each Ar charge state traveled since

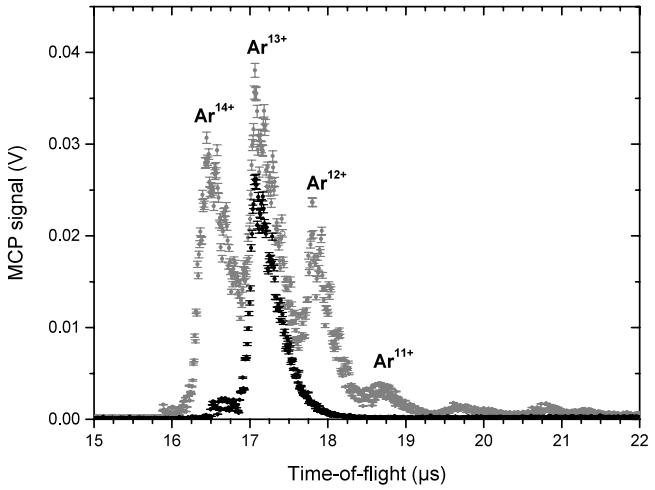

FIG. 7. Time-of-flight spectra measured with the MCP behind the Paul trap. The time starts at the moment of HCI extraction from the ion source. Grey data points are the spectrum without use of the kicker electrode and for an applied e^--beam acceleration voltage of 997 V. Black data points describe the spectrum obtained with using the kicker electrode to exclude lower charge states than Ar^{13+} and an applied e^--beam acceleration voltage of 777 V to suppress higher charge states. Spectra taken without EBIT residual magnetic field compensation.

extraction and hence to a specific retarding potential the ion experienced at pulse-down time.

Deceleration scans, where we vary the pulse-down time and measure the TOF spectrum, are shown in Figs. 9 and 10, respectively. The case where both serrated electrodes are initially set to the same retarding potential is shown in Fig. 9, while Fig. 10 displays the case where the second pulsed drift tube is initially placed at a higher potential than the first one (as seen by the incoming HCIs). The vertical coordinate axis of the displayed intensity plots shows the measured TOF spectrum averaged over 64 extracted HCI pulses, containing different charge states of argon. Since the kinetic energy of the ions after extraction is directly proportional to their charge state, ions with higher charge state are faster and arrive earlier at the detector. The horizontal axis is the pulse-down time t_S which is increased stepwise, so that, e.g., the dotted white curves in Figs. 9 and 10 result from Ar^{13+} ions.

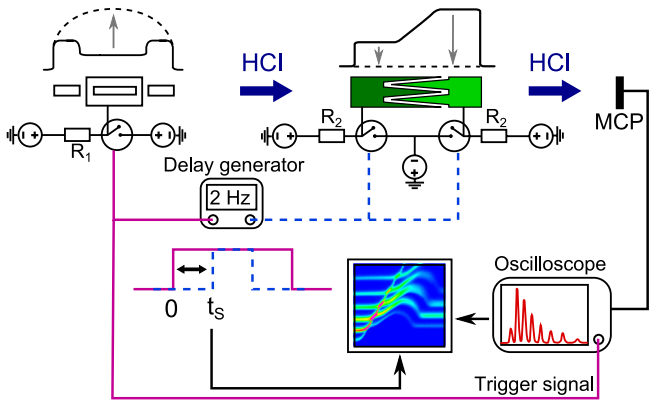

FIG. 8. Data acquisition scheme used for commissioning the deceleration properties of the beamline and experimentally determining suitable pulse-down times t_S for the interlaced serrated electrodes.

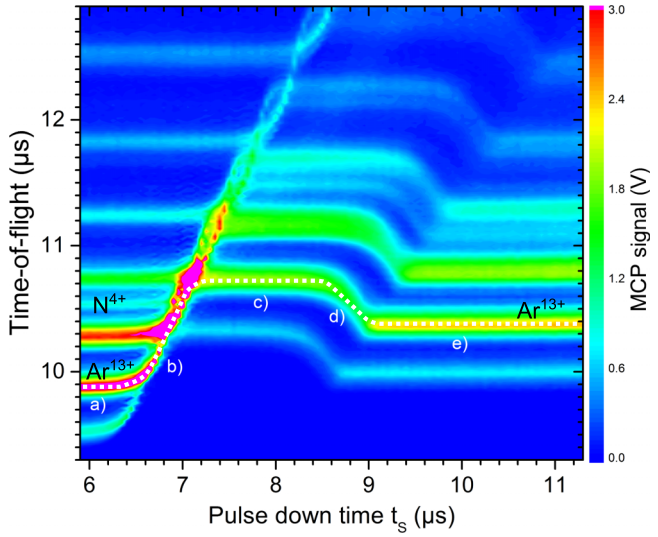

FIG. 9. Exemplary deceleration scan for extracted HCI pulses. Argon charge states from 14 to 8 elementary charges are displayed. The white dotted curve represents the mean time-of-flight for Ar^{13+} ions for a scan of the pulse-down time. Initial decelerating voltages applied to the serrated electrodes are $V_{PDT1} = V_{PDT2} = 300$ V, while the HCI bunch is extracted with an approximate mean kinetic energy of 685 eV/Q. Labels (a) through (e) mark different parts of the deceleration process and are explained in the main text. Each TOF spectrum is averaged over 64 extraction cycles. Spectra recorded without compensation coils ((CCs) in Fig. 1) in place.

The t_S range marked with (a) in Figs. 9 and 10 corresponds to constant TOF values of the Ar^{13+} ion pulse. This is due to the pulsed drift tubes already being at ground potential when the ions enter them. For larger pulse-down times the ions start to enter the first pulsed drift tube. For even larger values in t_S the Ar^{13+} ions have been decelerated further and further at

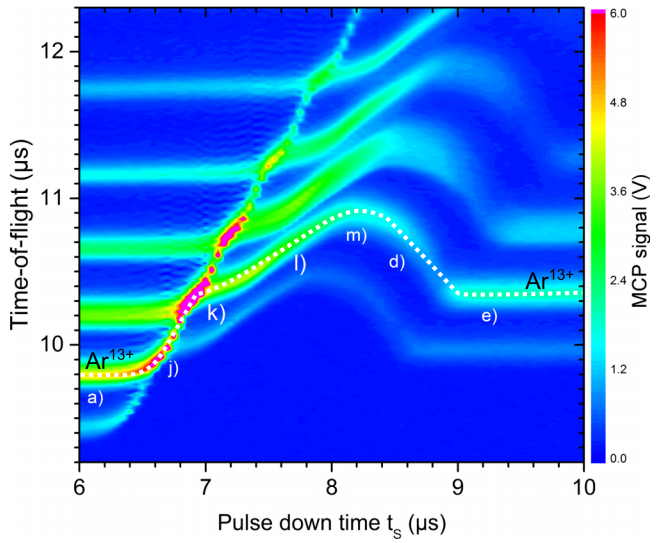

FIG. 10. Exemplary deceleration scan with precooling for extracted HCI pulses. Argon charge states from 14 to 9 elementary charges are displayed. The white dotted curve represents the mean time-of-flight for Ar^{13+} ions for a scan of the pulse-down time. Initial decelerating voltages applied to the serrated electrodes are $V_{PDT1} = 200$ V and $V_{PDT2} = 400$ V, respectively. The HCI bunch is extracted with mean kinetic energy of 695 eV/Q. Each TOF spectrum is averaged over 64 extraction cycles. See main text for explanation of labels. Spectra recorded without compensation coils ((CCs) in Fig. 1) in place.

pulse-down by the decelerating potential of the first pulsed drift tube, resulting in a steady increase of their time-of-flight (labeled with (b) and (j) in Figs. 9 and 10, respectively). This process ends when the ions either enter the range of constant potential ((c) in Fig. 9) within the pulsed drift tubes where their TOF remains constant or they transition into the beginning of the linearly increasing decelerating potential within the interlaced region of the two PDTs (t_S regimes (k) and (l) in Fig. 10). Here, (m) marks the t_S values that correspond to the ions leaving the interlaced region of the two serrated electrodes. For pulse-down times that correspond to the ions exiting the second electrode (region (d) in Figs. 9 and 10), the ions are again accelerated by rolling down the potential hill to a certain amount before pulsedown. At t_S values labeled (e) in Figs. 9 and 10 the HCI pulse has already exited the second pulsed drift tube at pulse-down. Here, the time-of-flights of the HCIs are larger compared to those in (a). This is due to the fact that both pulsed drift tubes act as one long Einzel lens on a positive potential. The kinetic energy of the HCI pulse is unchanged after the ions flew through the electrodes, but their TOF increases. This is because they travel the distance within the electrodes with lower velocity compared to the case (a) where both electrodes are on ground when the ions fly through them.

The deceleration scans can be used to probe the form of the electric potential generated by the voltages applied to the two pulsed drift tubes, as demonstrated by Figs. 9 and 10. In addition, they yield ranges for suitable pulse-down times and are thus an essential part of the commissioning process. This method for determining a suitable value of t_S is not effected by the extraction or charge state selection process.

The width of the coloured curves in the deceleration scans corresponds to the width of the ion pulses with specific Q/M ratio. This temporal width is a measure for the kinetic energy spread in the pulse relative to its mean kinetic energy. The pulse width in region (l) of Fig. 10 is not larger than the one in region (a) despite the lower mean kinetic energy in (l) compared to the initial mean kinetic energy in (a). This is only possible if a compression of the longitudinal kinetic energy has been achieved and is thus proof for the precooling properties of the beamline.

For a quantitative analysis, we compare the measured temporal width of Ar^{13+} ions in Fig. 10 with theoretical temporal width calculated by employing the model presented in Section III C. Using the experimental TOF spectra at t_S = 6 μs and t_S = 7.6 μs for the analysis yields an experimentally observed reduction in kinetic energy spread of the Ar^{13+} ion bunch by a factor of 2. This is anticipated by the theoretical model of Section III C, since the optimal precooling voltages (V_{PDT1}, V_{PDT2}) for the combination of an initial extraction energy of 695 eV/Q and a target kinetic energy of 395 eV/Q are about (237 V, 363 V).

Ar^{13+} ion bunches used for the measurement campaign around the retrapping of HCIs, described in Section IV, have been decelerated and precooled to a mean kinetic energy of 130.6 eV/Q and FWHM energy spread of 7.1 eV/Q by employing precooling voltages (V_{PDT1}, V_{PDT2}) of (450 V, 650 V). Analyzing the area under the MCP ion signal, which is linked to the number of ions impinging onto the detector, gives a rough estimate for the absolute number of Ar^{13+} ions in those precooled and decelerated bunches of 1.3×10^4. This is about 50% of the value typically measured for undecelerated Ar^{13+} ion bunches.

IV. RETRAPPING HCIS IN A LINEAR PAUL TRAP

Being able to retrap the HCIs in the linear Paul trap for several ms proved to be a necessary prerequisite to provide sufficient interaction time for sympathetic cooling in a Be^+ ion crystal. The demonstration of such long trapping times (without a Be^+ ion crystal present) allows for multiple passes through laser-cooled Be^+ Coulomb crystals in the next step and thus increases the probability for stopping HCIs in them.

The retrapping process is schematically shown in Fig. 11. First, in the injection phase all Paul trap electrodes (pretrap electrodes (b) and main trap electrodes (c)) are commonly biased to typically 130 V, while the 1st (a) and 2nd (d) electrostatic mirror electrodes in coaxial arrangement are placed at ground and 200 V, respectively. In this way, the previously decelerated ion bunch just overcomes the electrostatic retarding potential formed by all Paul trap electrodes. Subsequently the HCIs travel inside the trap with residual kinetic energies below 1 eV/Q. Prior to the HCI injection phase, the mean kinetic energy of the HCI bunch is determined with the retarding field analyzer ((BD1) in Fig. 1) located directly after the deceleration beamline. This directly yields the value for the needed electrostatic retarding potential formed by the Paul trap electrodes. The 2nd electrostatic mirror electrode downstream stops and reverses the axial motion of the HCIs. Before they leave the trap, the 1st electrostatic mirror electrode is quickly pulsed to 200 V, a value that closes the trap. Thus, the now retrapped HCIs

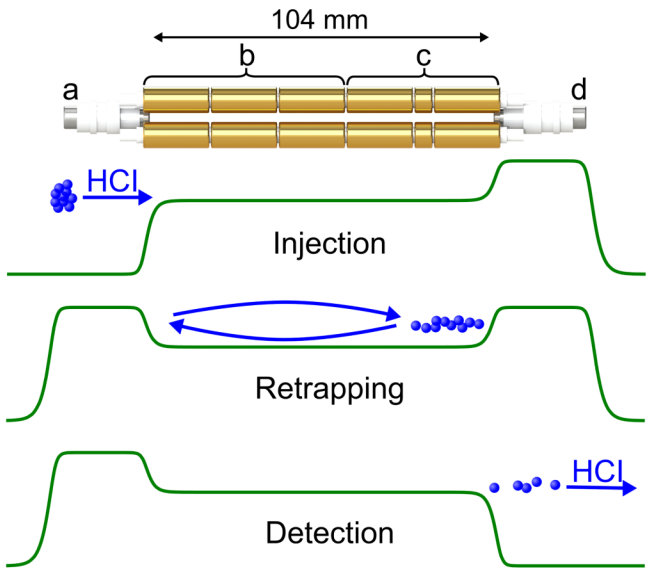

FIG. 11. Top to bottom: Schematic of retrapping electrodes followed by DC potential curves along the Paul trap symmetry axis sequentially applied to the electrodes during the retrapping measurements. Those consist of injection, retrapping, and detection phases. Electrodes: (a) and (d) are the hollow cylinder 1st and 2nd electrostatic mirror electrodes with 3 mm inner diameters, respectively. (b) and (c) label the Paul trap pre- and main-trap electrodes biased to a common retarding potential. This yields a volume of 140 mm × 28 mm^2 for retrapping HCIs in CryPTEx.

axially oscillate between the two mirror electrodes, since they are radially confined by the Paul trap radio frequency fields. The trap is opened after an adjustable delay time by quickly pulsing the voltage applied to the 2nd electrostatic mirror to ground, releasing the HCIs onto a MCP detector axially located behind (as seen by the HCIs coming from the EBIT) the Paul trap ((BD2) in Fig. 1). This enables us to analyze the retrapping process and to determine HCI, specifically Ar^{13+}, retrapping times. The number of HCIs caught depends decisively on the tuning of the EBIT and all beamline elements including the experimentally determined switching times of pulsed electrodes. The residual kinetic energy spread of the bunch together with the deceleration to kinetic energies below 10 eV leads to a relatively large temporal and longitudinal spatial spreadings of the HCI bunch inside the Paul trap. This fact in combination with a loss in particles during the ejection phase on the way to the MCP detector leads to counting of single or few HCIs. This is illustrated schematically in Fig. 11 and confirmed by retrapping measurements shown in Fig. 12.

Typical retrapping measurement series, as depicted in Fig. 12 start with a reference measurement without reflection cycle. This reference measurement is obtained by placing all Paul trap electrodes at a potential of, e.g., 130 V while the two electrostatic mirror electrodes are grounded. The fastest Ar^{13+} ions in the extracted ion bunch arrive at the MCP detector after 29.2 μs. The temporal spreading of the bunch is about 56 μs and thus roughly 28 times larger than the temporal spreading of HCI bunches that arrive at the detector when all Paul trap electrodes are placed at DC voltages of 0 V. This is due to the dispersion of the HCI bunch inside the Paul trap when all trap electrodes are biased to 130 V. Next, we apply the retrapping scheme of Fig. 11 while stepwise increasing the switching time of the 2nd mirror electrode. Increased pulse-down times, marked by arrows in Fig. 12, of the 2nd mirror electrode are correlated with delayed exiting of the captured HCIs from the

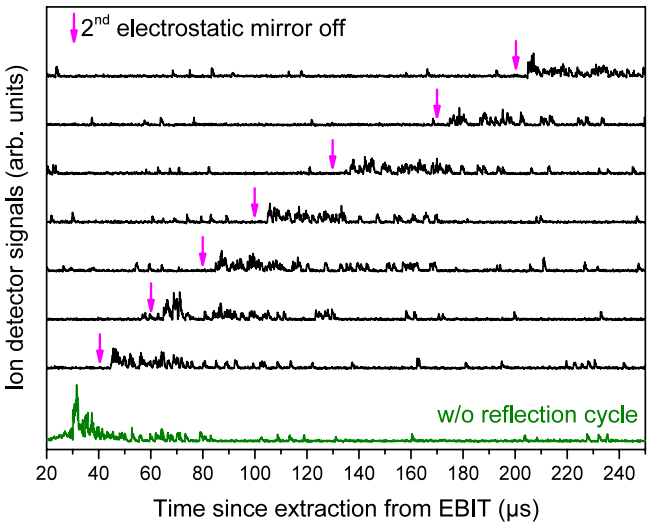

FIG. 12. Exemplary measurement series starting with a reference ion detector signal as a function of time-of-flight without reflection cycles (green trace at bottom). The time at which the retrapped Ar^{13+} ions are released in the direction of the MCP detector is marked with magenta arrows and increases from bottom to top. Each of the oscilloscope traces of the MCP signals is averaged over 32 retrapping cycles.

trap. The presence of HCI-induced MCP signals at times when only a background signal can be seen in the oscilloscope trace without reflection cycle indicates the successful retrapping of HCIs in the linear Paul trap. The time gap of 5 μs between the release of HCIs from the Paul trap (position of arrows in Fig. 12) and the first arrival of HCIs with minimum kinetic energy of 13×130 eV at the MCP detector is due to the distance of about 45 cm between the end of the Paul trap and the detector.

Retrapping of HCI bunches is achieved by the combination of axial confinement through the differently biased trap and mirror electrodes with the radial confinement by the Paul trap radio frequency (RF) field. CryPTEx is operated with a RF frequency $f_{RF} = \Omega_{RF}/2\pi$ of 3.92 MHz. The RF peak-to-peak voltage V_{RF} for the retrapping measurements presented here is 46 V. This corresponds to a radial Mathieu stability parameter[43] $q_r = 2QV_{RF}/(M\Omega_{RF}^2 r_0^2)$ for Ar^{13+} ions of $q_r = 0.39$. Here, $r_0 = 3.5$ mm is the minimum distance from the Paul trap electrodes to its axis. Assuming a harmonic motion in radial direction with trap frequency $\omega_r = q_r\Omega_{RF}/(2\sqrt{2})$ yields an upper limit for the Q^2/M-dependent radial well depth U_r of our Paul trap of[43]

$$U_r = 0.5M\omega_r^2 r_0^2. \quad (7)$$

Eq. (7) gives a value of 29 eV for the radial well depth for Ar^{13+} ions for typical drives of the RF-field used during the retrapping process, corresponding to an upper limit for the transverse energy acceptance of our Paul trap for Ar^{13+} ions. In axial direction, slow (longitudinal injection energies below 10 eV) Ar^{13+} ions will be reflected by the potential difference of 70 V between the mirror electrodes and the Paul trap electrode bias, which determines the longitudinal energy acceptance of our Paul trap setup.

We record different oscilloscope traces of the ions MCP signal for the unambiguous demonstration of successful retrapping of Ar^{13+} ions in a linear Paul trap as shown in Fig. 13. First, we choose a value for the pulse-down time of the 2nd mirror electrode and record a TOF spectrum with reflection cycles for reference (red graph). Next, we leave the 1st mirror electrode at ground potential for the whole measurement so that captured HCIs can leave the trap again in the reversed direction and can only be reflected once by the 2nd mirror electrode (orange graph). After that we perform a measurement applying the full retrapping scheme with the exception of turning off the radio frequency of the Paul trap and thus the radial confinement (blue graph). Finally, we apply the full retrapping scheme but tune the nearly mono-energetic electron beam of the EBIT to an energy below the ionization potential of Ar^{12+} in order to turn off the production of Ar^{13+} ions (black graph). In all three comparison measurements only background signal could be detected. This is proof of the retrapping of Ar^{13+} ions in a linear Paul trap. Retrapping times up to 70 ms could be observed for the given experimental settings.

The number of Ar^{13+} ions detected with (BD2) can be determined by calibrating the area under the MCP ion signal. We analyze this number for the retrapping measurements shown in Fig. 12 together with one for longer retrapping times form the same measurement series. The time interval for the

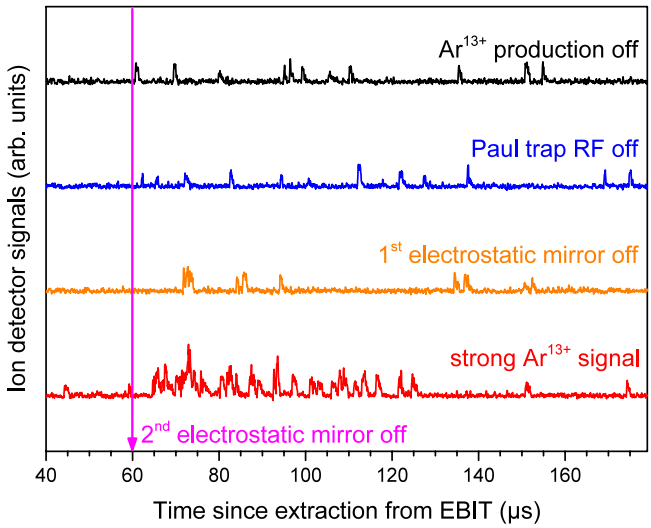

FIG. 13. Oscilloscope traces of ion detector signal recorded for the unambiguous demonstration of successful retrapping of Ar^{13+} ions in a linear Paul trap. The red trace at bottom comes from application of the full retrapping scheme for a pulse-down time of 60 μs for the voltage of the 2nd mirror electrode. The other detector signals are recorded while selectively turning off elements of the retrapping scheme. Each of the oscilloscope traces of the MCP signals is averaged over 32 retrapping cycles.

reference measurement without reflection cycle is 56 μs long and starts at 29.2 μs. Analysis of the detector signals with reflection cycle is based on 90 μs long time windows starting when the 2nd mirror electrode is pulsed down (magenta arrows in Fig. 12). First, we determine mean and standard deviation of the areas under 40 clearly resolved single ion peaks that occur outside the evaluated time intervals. Subsequently, we divide the areas under the unresolved ion signals within the time windows by the single ion peak value to obtain the number of detected ions under assumption of linearity. The results, which are depicted in Fig. 14, yield a lower limit for the ion numbers since extraction losses cannot be determined with the current setup and are thus not taken into account. No dependence between the number of retrapped HCIs and their retrapping time is observed. Thus, comparing mean and standard deviation of the eight retrapping measurements in

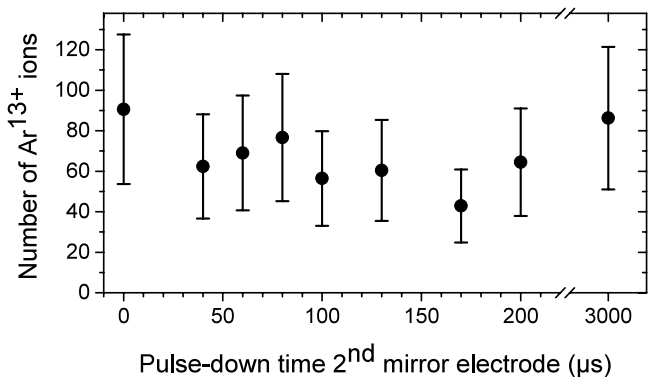

FIG. 14. Number of Ar^{13+} ions detected with (BD2) against pulse-down time of the 2nd mirror electrode for the oscilloscope traces in Fig. 12. The time 0 μs corresponds to the reference measurement without reflection cycle. Error bars stem from the standard deviation of the single ion peak analysis. Ion extraction losses cannot be determined experimentally with the current setup and are thus not taken into account in the data analysis.

Fig. 14 of 68(15) Ar^{13+} ions with the 91(37) Ar^{13+} ions arriving at (BD2) for the reference measurement yields that 75(17)% of the transmitted ions can be recaptured by the Paul trap for the given experimental settings.

We perform SIMION simulations (including micromotion) of the retrapping process for HCIs that are injected off-axis and analyze the geometrical acceptance of our linear Paul trap. Therefore, we import the CAD electrode geometry of the Paul trap in combination with the electrostatic mirrors and a grounded housing into SIMION. Here, we are able to individually set the RF drive and DC values of all Paul trap electrodes as well as the voltages, pulse-down times, and time constants for the electrostatic mirrors. We employ simulation parameters that are close to the experimental ones: a RF peak-to-peak voltage of 50 V at $f_{RF} = 3.92$ MHz, a Paul trap DC bias of 133 V, the 1st electrostatic mirror is switched from ground to 220 V with a time constant of 0.1 μs, a potential difference between the middle and outer main trap electrodes of 0.6 V.

We simulate the percentage of Ar^{13+} ions that exit the Paul trap after a potential exemplary retrapping time of 500 μs in dependence of their longitudinal kinetic energy (collimated beam — no divergence) and off-axis starting position before injection. At least 50 ions per kinetic energy and starting position are flown with random phases in regard to the Paul trap radiofrequency field. In these simulations, 100% of Ar^{13+} ions injected with kinetic energies of 133 eV/Q to 134 eV/Q that are started within a diameter of 450 μm around the central trap axis are retrapped for the probed 500 μs retrapping time.

The percentage of retrapped Ar^{13+} ions decreases to 5% when the diameter is increased from 450 μm to 1.3 mm around the trap axis. Adding a 1° half-angle divergence equal distribution (which is the upper limit of the experimentally expected divergence) to every starting position results in retrapping an average of (5 ± 3)% of Ar^{13+} ions that are injected within a diameter of 3 mm.

Finally, we simulate the number of reflections N within the Paul trap together with the corresponding retrapping times of recaptured Ar^{13+} ions in dependence of their longitudinal kinetic energy at injection with the electrode settings as described above. The Ar^{13+} ions are injected on-axis with random phases in regard to the RF field of the Paul trap. The trajectory of one Ar^{13+} ion per energy step of 0.1 eV is simulated. The ions time-of-flight is recorded, whenever it passes a plane perpendicular to the trap axis in the middle between the two electrostatic mirrors. Thus, the number of records per ion gives N, while the difference between the first and last recorded TOF yields the retrapping time. The results of this exemplary simulation are shown in Fig. 15.

The separate peaks for higher injection energies that transition into a continuum for smaller values appear to be due to a stability condition for the reflection trajectories. For the peak positions, this condition can be modeled by assuming that the geometric distance L between the turning points is restricted to be an integer multiple of the half-wavelength $\lambda/2 = \pi v_{HCI}/\omega_r$ of the path that the ions trace out in the pseudopotential of the Paul trap: $L = n\lambda/2, n \in \mathbb{N}$. Here $v_{HCI} = \sqrt{2E_{HCI}/M}$ is the longitudinal velocity of the Ar^{13+} ion that has been injected into the Paul trap with a longitudinal kinetic energy of E_{HCI}. In conclusion, the simulated spectra of

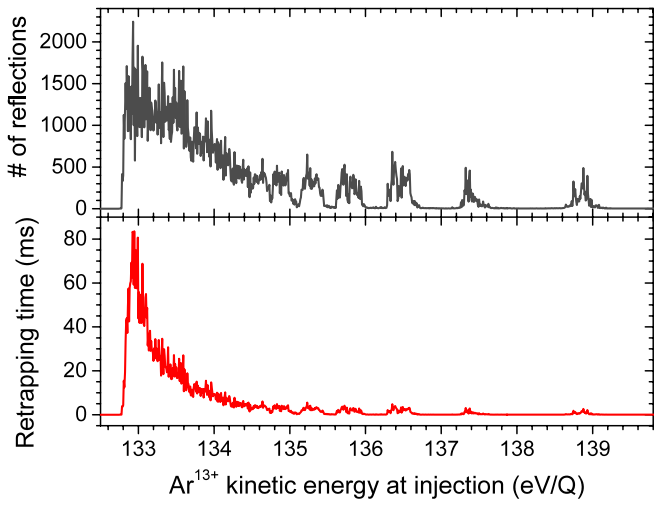

FIG. 15. Top: SIMION simulated number N of reflections within the Paul trap of recaptured Ar^{13+} ions in dependence of their kinetic energy at injection. Bottom: Simulated retrapping times of Ar^{13+} ions, corresponding to the number of reflections shown in the top graph, in dependence of their kinetic energy at injection. Ions are injected on-axis into the Paul trap, which is DC-biased to 133 V and driven with a RF-voltage of $V_{RF} = 50$ V ($q_r(Ar^{13+}) = 0.42$, $\omega_r/2\pi = 585$ kHz). Retrapping of ions with injection energies barely below E_0 is due to accelerating effects from the RF-field in combination with the pulse-up of the 1st mirror electrode.

the number of reflections of retrapped HCIs show resonances around specific injection energies, given by the condition

$$E_{HCI} = \frac{M\omega_r^2 L^2}{2\pi^2 n^2}. \quad (8)$$

Simulations of ion trajectories with different injection energies show a weak dependence of L on the injection energy. This can be expected, since the motion of slower ions can be reversed by smaller reflecting potentials.

The retrapping time t_{rt} of a HCI is linked to the number of reflections N and the energy difference between the injection energy E_{HCI} and the energy equivalence $E_0 = QV_{bias}$ of the Paul trap DC bias V_{bias} by the proportionality $t_{rt} \propto N/\sqrt{E_{HCI} - E_0}$. This directly yields the steep increase in retrapping time towards small injection energies as depicted in Fig. 15.

Finally, we compare the experimentally measured retrapping times of up to 70 ms with the ones in Fig. 15, which are simulated under similar retrapping parameters. This leads to the conclusion that the experimental kinetic energies of the retrapped Ar^{13+} ion ensemble have to be below 10 eV to optimize retrapping.

V. STOPPING HCIS IN LASER-COOLED BE$^+$ COULOMB CRYSTALS

For implanting HCIs in a Be^+ ion crystal, we tune all EBIT and beamline parameters to achieve successful retrapping of the HCIs in the Paul trap without the presence of Be^+ ions in the trap. After that, we start a stopping sequence: First, we load singly ionized Be in the Paul trap by resonance-enhanced two-photon ionization[44] of neutral Be atoms, which are evaporated from an atomic oven source. Then we cool the Be^+ ion one-component plasma with one cooling laser beam at 313 nm (near resonant with the $2\,^2S_{1/2}, F = 2 \leftrightarrow 2\,^2P_{3/2}, F = 3$ transition) in combination with a repumping laser beam (red detuned by 1.25 GHz to repump population from the $2\,^2S_{1/2}, F = 1$ to the $2\,^2P_{3/2}$, $F = 3$ states) along the trap axis until the plasma is strongly coupled and undergoes a phase transition to the crystalline state. As a result we are able to image the fluorescing Be^+ Coulomb crystal onto an image-intensified CCD camera (Andor iStar 740). Details about the photoionization of Be atoms and laser cooling of Be^+ ions can be found in the supplementary material in Ref. 27 and in Ref. 45. Subsequently, we inject the decelerated and pre-cooled HCI bunches, coming from the EBIT into the Paul trap and apply the retrapping scheme. In the Paul trap the HCIs can be stored together with the Be^+ ions since the HCIs mass-to-charge-ratio differs less than a factor of three from the one of the Be^+ ions. In the sympathetic cooling scheme, long-range elastic Coulomb collisions with the continuously laser-cooled Be^+ ions drive the HCI temperature down to the mK range[27] (kinetic energies on the μeV/Q scale). However, the co-crystallized HCIs do not scatter light from the cooling laser and therefore form dark round structures within the bright fluorescing Be^+ ensemble as shown in Fig. 16.

The location after crystallization of the HCIs with respect to the Be^+ ions is the result of the minimization of the total energy of the two-species ion ensemble within the trap potentials. Ions with a smaller M_{HCI}/Q_{HCI} experience a steeper radial pseudopotential[43] due to the trapping fields (e.g., $V_{RF} = 50$ V) than ions with a larger mass-to-charge-ratio and thus crystallize along the trap axis. Assuming the Be^+ ions are cooled to a crystal first, the position of a few HCIs along the trap axis would additionally be influenced by the space-charge of the Be^+ ions, since the axial trapping field (e.g., V_{DC} is on the order of a few 100 mV) is considerably weaker than the radial ones. In this case, Ar^{13+} ions would be expected to be preferably located on either side of the Be^+ ion crystal. The asymmetric distribution of a few Ar^{13+} ions along the trap axis in Fig. 16 stems basically from the combination of two effects. In separate measurements we have observed the presence of axial excess micromotion[46] along the trap major axis, which is possibly due to imperfectly applied RF voltages. Its velocity amplitude increases from right to left in Fig. 16, resulting in a ponderomotive force along the trap major axis. This force increases for higher charge states and thus pushes the HCIs to the right. Additionally, we used only one cooling laser along the axis (impinging from the right in Fig. 16). Thus, radiation pressure solely acts on the laser-cooled Be^+ ions and pushes

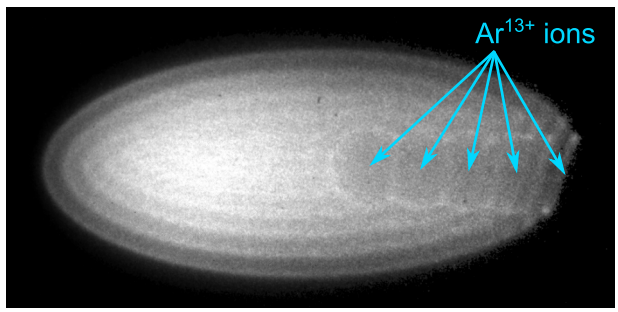

FIG. 16. CCD fluorescence image of five non-scattering Ar^{13+} ions (positions marked by arrows) implanted in a continuously laser-cooled 1 mm-sized Be^+ Coulomb crystal consisting of about 1500 Be^+ ions.

them to the left in Fig. 16. The effect due to axial excess micromotion is the dominant one, since shining in the cooling laser from the other side leads to a less asymmetric but still not symmetric distribution of a few Ar^{13+} ions along the trap axis.

Unambiguous charge state identification of the co-crystallized dark ions has been described in Ref. 27 and is in accord with a charge state of $13e$ as expected from TOF spectra. Trapping times for the co-crystallized Ar^{13+} ions are in excess of 15 min. No charge exchange of HCIs with residual gas, signified by a reduction in diameter of the dark circular shapes around HCI equilibrium positions, could be observed under normal vacuum conditions.

Typical HCI loading rates range from 1 s^{-1} to 15 s^{-1}. Stacking of HCIs is possible and has been used to co-crystallize more than 20 Ar^{13+} ions. During the measurement campaign around Fig. 12 we have observed loading rates from 5 s^{-1} to 10 s^{-1}. We extract HCIs with a frequency of 2 Hz from the EBIT. Thus we are repeatedly able to retrap on the order of 68(15) Ar^{13+} ions (compare Fig. 14) for 70 ms within this 2 Hz extraction cycle. This corresponds to (6–19)% of the retrapped Ar^{13+} ions being actually stopped and co-crystallized by the Be^+ Coulomb crystal for the given experimental settings. Under our normal working conditions, these loading rates are not needed, since we trap Ar^{13+} ions aiming at laser-induced fluorescence spectroscopy or quantum logic readout, respectively.

We observe no significant loss of Be^+ ions during the stopping process. On the CCD image exposure time scale above 0.5 s, the Be^+ ions remain within the acceptance of the laser force and are not taken out of resonance with the cooling laser due to energy transfer from the HCIs to the Be^+ ions. This indicates that the energy deposited in the Coulomb crystal is distributed over a large plasma volume and quickly cooled away by the Doppler cooling laser.

VI. CONCLUSION

The presented method for deceleration, precooling, and multi-pass stopping of HCIs in Be^+ Coulomb crystals is based on external ion injection into a linear Paul trap. This holds the advantages that the production mechanism can be chosen or switched so that it is most suitable for the ion under study and that the properties of the ion bunches can be manipulated prior to injection. We developed specifically shaped time-varying electric fields for longitudinal phase-space manipulation of extracted HCI pulses. Compression of the longitudinal kinetic energy spread can be achieved due to the correlation between ion position and kinetic energy within the interlaced region of the two serrated pulsed electrodes. Using simulations and an analytical one-dimensional model, we determined both the optimal geometry of the pulsed electrodes and the applicable voltage range for precooling. Other manipulation mechanisms are readily conceivable, e.g., the use of a pulsed hollow cone electrode to reduce the transverse divergence in an ion bunch.

Careful ion bunch alignment together with an appropriate manipulation of its kinetic energy distribution enabled retrapping Ar^{13+} ions for up to 70 ms in a linear Paul trap in the absence of sympathetic cooling. This rendered the stopping of HCIs in laser-cooled Be^+ ions possible. Eventually, the combination of an EBIT with a cryogenic linear Paul trap by means of a beamline with deceleration, precooling, and multi-pass stopping properties facilitated the formation of 3- and 1-dimensional mixed-species Coulomb crystals.[27]

Our versatile technique for the preparation of cold HCIs opens new possibilities for fundamental research. One application could be the realization of novel optical clocks with a projected stability of 10^{-19} or better. This very small measurement uncertainty in conjunction with their identification as sensitive probes for possible variation of the fine structure constant makes HCIs ideal candidates for putting tighter limits on such possible drifts.

ACKNOWLEDGMENTS

We thank the MPIK mechanical workshops. Financial support was provided by DFG through the Center for Quantum Engineering and Space-Time Research (QUEST).

[1]J. K. Webb, J. A. King, M. T. Murphy, V. V. Flambaum, R. F. Carswell, and M. B. Bainbridge, Phys. Rev. Lett. **107**, 191101 (2011).
[2]J. C. Berengut and V. V. Flambaum, EPL **97**, 20006 (2012).
[3]T. Nicholson, S. Campbell, R. Hutson, G. Marti, B. Bloom, R. McNally, W. Zhang, M. Barrett, M. Safronova, G. Strouse *et al.*, Nat. Commun. **6**, 6896 (2015).
[4]N. Huntemann, B. Lipphardt, C. Tamm, V. Gerginov, S. Weyers, and E. Peik, Phys. Rev. Lett. **113**, 210802 (2014).
[5]R. M. Godun, P. B. R. Nisbet-Jones, J. M. Jones, S. A. King, L. A. M. Johnson, H. S. Margolis, K. Szymaniec, S. N. Lea, K. Bongs, and P. Gill, Phys. Rev. Lett. **113**, 210801 (2014).
[6]C. Chou, D. Hume, J. Koelemeij, D. Wineland, and T. Rosenband, Phys. Rev. Lett. **104**, 070802 (2010).
[7]J. C. Berengut, V. A. Dzuba, V. V. Flambaum, and A. Ong, Phys. Rev. Lett. **106**, 210802 (2011).
[8]V. I. Yudin, A. V. Taichenachev, and A. Derevianko, Phys. Rev. Lett. **113**, 233003 (2014).
[9]M. S. Safronova, V. A. Dzuba, V. V. Flambaum, U. I. Safronova, S. G. Porsev, and M. G. Kozlov, Phys. Rev. Lett. **113**, 030801 (2014).
[10]A. Derevianko, V. A. Dzuba, and V. V. Flambaum, Phys. Rev. Lett. **109**, 180801 (2012).
[11]V. A. Dzuba, A. Derevianko, and V. V. Flambaum, Phys. Rev. A **86**, 054501 (2012).
[12]A. Windberger, J. R. Crespo López-Urrutia, H. Bekker, N. S. Oreshkina, J. C. Berengut, V. Bock, A. Borschevsky, V. A. Dzuba, E. Eliav, Z. Harman *et al.*, Phys. Rev. Lett. **114**, 150801 (2015).
[13]S. Bashkin, Science **148**, 1047–1053 (1965).
[14]E. Träbert, in *Trapping Highly Charged Ions: Fundamentals and Applications*, edited by J. Gillaspy (Nova Science Publisher, Inc., 2001).
[15]V. Mäckel, R. Klawitter, G. Brenner, J. R. Crespo López-Urrutia, and J. Ullrich, Phys. Rev. Lett. **107**, 143002 (2011).
[16]K. Schnorr, V. Mäckel, N. S. Oreshkina, S. Augustin, F. Brunner, Z. Harman, C. H. Keitel, J. Ullrich, and J. R. Crespo López-Urrutia, Astrophys. J. **776**, 121 (2013).
[17]T. Brunner, M. Smith, M. Brodeur, S. Ettenauer, A. Gallant, V. Simon, A. Chaudhuri, A. Lapierre, E. Mane, R. Ringle *et al.*, Nucl. Instrum. Methods Phys. Res., Sect. A **676**, 32–43 (2012).
[18]A. Kellerbauer, T. Kim, R. Moore, and P. Varfalvy, Nucl. Instrum. Methods Phys. Res., Sect. A **469**, 276–285 (2001).
[19]C. Droese, S. Eliseev, K. Blaum, M. Block, F. Herfurth, M. Laatiaoui, F. Lautenschläger, E. Minaya Ramirez, L. Schweikhard, V. Simon *et al.*, Nucl. Instrum. Methods Phys. Res., Sect. B **338**, 126–138 (2014).
[20]X. Fléchard, E. Liénard, A. Méry, D. Rodríguez, G. Ban, D. Durand, F. Duval, M. Herbane, M. Labalme, F. Mauger *et al.*, Phys. Rev. Lett. **101**, 212504 (2008).
[21]N. Scielzo, G. Li, M. Sternberg, G. Savard, P. Bertone, F. Buchinger, S. Caldwell, J. Clark, J. Crawford, C. Deibel *et al.*, Nucl. Instrum. Methods Phys. Res., Sect. A **681**, 94 (2012).

[22]A. Wagner, S. Sturm, F. Köhler, D. A. Glazov, A. V. Volotka, G. Plunien, W. Quint, G. Werth, V. M. Shabaev, and K. Blaum, Phys. Rev. Lett. **110**, 033003 (2013).
[23]L. Gruber, J. P. Holder, J. Steiger, B. R. Beck, H. E. DeWitt, J. Glassman, J. W. McDonald, D. A. Church, and D. Schneider, Phys. Rev. Lett. **86**, 636–639 (2001).
[24]M. Vogel, H. Häffner, K. Hermanspahn, S. Stahl, J. Steinmann, and W. Quint, Phys. Rev. A **90**, 043412 (2014).
[25]U. Chowdhury, M. Good, B. Kootte, D. Lascar, B. E. Schultz, J. Dilling, and G. Gwinner, AIP Conf. Proc. **1640**, 120 (2015).
[26]D. J. Larson, J. C. Bergquist, J. J. Bollinger, W. M. Itano, and D. J. Wineland, Phys. Rev. Lett. **57**, 70–73 (1986).
[27]L. Schmöger, O. Versolato, M. Schwarz, M. Kohnen, A. Windberger, B. Piest, S. Feuchtenbeiner, J. Pedregosa-Gutierrez, T. Leopold, P. Micke, A. Hansen, T. Baumann, M. Drewsen, J. Ullrich, P. Schmidt, and J. Crespo López-Urrutia, Science **347** (2015).
[28]M. Schwarz, O. O. Versolato, A. Windberger, F. R. Brunner, T. Ballance, S. N. Eberle, J. Ullrich, P. O. Schmidt, A. K. Hansen, A. D. Gingell *et al.*, Rev. Sci. Instrum. **83**, 083115 (2012).
[29]P. O. Schmidt, Science **309**, 749–752 (2005).
[30]R. Marrs, Nucl. Instrum. Methods Phys. Res., Sect. B **149**, 182–194 (1999).
[31]M. Bussmann, U. Schramm, D. Habs, V. Kolhinen, and J. Szerypo, Int. J. Mass Spectrom. **251**, 179 (2006).
[32]P. Mandal, G. Sikler, and M. Mukherjee, J. Instrum. **6**, P02004–P02004 (2011).
[33]H. D. Zeman, Rev. Sci. Instrum. **48**, 1079 (1977).
[34]A. Ghalambor-Dezfuli, R. Moore, and S. Schwartz, Rev. Sci. Instrum. **73** (2002).
[35]S. Coeck, B. Delaure, M. Herbane, B. Beck, V. Golovko, S. Kopecky, V. Kozlov, I. Kraev, A. Lindroth, and T. Phalet, Nucl. Instrum. Methods Phys. Res., Sect. A **572**, 585 (2007).
[36]W. B. Colson, J. McPherson, and F. T. King, Rev. Sci. Instrum. **44**, 1694 (1973).
[37]S. Goldberg, D. Strasser, O. Heber, M. L. Rappaport, A. Diner, and D. Zajfman, Phys. Rev. A **68**, 043410 (2003).
[38]I. Wolfram Research, *Mathematica*, version 10.2 ed. (Wolfram Research, Inc., Champaign, Illinois, 2015).
[39]D. A. Dahl, Int. J. Mass Spectrom. **200**, 3–25 (2000).
[40]L. Nagel and D. Pederson, Memorandum No. ERL-M382, University of California, Berkeley, 1973.
[41]S. Mahmood, S. Ali, I. Orban, S. Tashenov, E. Lindroth, and R. Schuch, Astrophys. J. **754**, 86 (2012).
[42]J. R. Crespo López-Urrutia, J. Braun, G. Brenner, H. Bruhns, A. Lapierre, A. J. Gonzalez Martinez, V. Mironov, R. Soria Orts, H. Tawara, M. Trinczek *et al.*, Rev. Sci. Instrum. **75**, 1560 (2004).
[43]M. Drewsen and A. Broner, Phys. Rev. A **62**, 045401 (2000).
[44]N. Kjaergaard, L. Hornekaer, A. Thommesen, Z. Videsen, and M. Drewsen, Appl. Phys. B **71**, 207 (2000).
[45]H.-Y. Lo, J. Alonso, D. Kienzler, B. C. Keitch, L. E. de Clercq, V. Negnevitsky, and J. P. Home, Appl. Phys. B **114**, 17 (2013).
[46]D. J. Berkeland, J. D. Miller, J. C. Bergquist, W. M. Itano, and D. J. Wineland, J. Appl. Phys. **83**, 5025 (1998).